Journal of
Materials Chemistry A

ROYAL SOCIETY
OF CHEMISTRY

PAPER

View Article Online
View Journal

Check for updates

Cite this: DOI: 10.1039/d5ta07799k

Decoupling the capacity fade contributions in polymer electrolyte-based high-voltage solid-state batteries

Ji-young Ock, *[a] Sergiy Kalnaus, [b] Michael J. Zachman, [c] Andrew M. Ullman,[a] Kyra D. Owensby,[ad] Oliver Long,[a] Xi Chelsea Chen *[a] and Ritu Sahore *[a]

Received 23rd September 2025
Accepted 26th November 2025

DOI: 10.1039/d5ta07799k

rsc.li/materials-a

Polymer electrolyte (PE)-based solid-state batteries (PE-SSBs) made with high-voltage cathodes are known to suffer from severe capacity fade, stemming primarily from the poor oxidative stability of most PEs under high-voltage cycling conditions. PEs also suffer from greater ion-transport limitations compared to liquid or solid electrolytes. However, often, these limitations are collectively stated to be responsible for the observed capacity fade, and it is challenging to decouple the contributions of different factors. Herein, a tunable cell fabrication platform was developed to systematically investigate and decouple the two primary capacity fade drivers (cell impedance growth and kinetic limitations), while keeping the other cell parameters constant. Three PE types with distinct transport characteristics were compared. By utilizing a voltage profile analysis method, the contribution of the cell's internal impedance growth was quantitatively decoupled from the kinetic limitations stemming from the high concentration gradient in the polymer catholyte and slow charge transfer reactions. We demonstrate that the high interfacial impedance did not necessarily correlate with the high capacity fade rate. Kinetic limitations that are not reflected by impedance measurements can play a dominant role in causing cumulative capacity decay.

1. Introduction

Demand for batteries with higher energy density and safety has revitalized solid-state battery (SSB) research.[1,2] Polymer electrolyte (PE)-based SSBs (PE-SSBs) are promising candidates because of their processibility and the potential to address the low-pressure requirements of all-inorganic solid-state batteries (SSBs).[3,4] The elastic and adhesive properties of PEs can help maintain electrode/electrolyte interfacial contacts during low-pressure cycling.[5–8] However, the low room temperature (RT) ionic conductivity, low Li^+ transference number (t_+), and low oxidative stability of most PEs remain their significant drawbacks.[9–13] Poor bulk ion-transport kinetics hampers the rate capability of cells, especially with thick (practical) cathodes. Poor oxidative stability leads to fast impedance growth at the cathode–electrolyte interface (CEI) when paired with energy-dense, high-voltage cathodes, causing a dramatic capacity fade of such PE-SSBs.[12,13]

In addition to poor rate capability, ion-transport limitations also result in accelerated capacity fade. For example, in lithium-ion batteries with liquid electrolytes, where transport limitations become relevant at high C-rates (0.5–5 C), faster capacity fade has been shown to occur as the cathode thickness increases.[14–17] The Li^+ ion diffusion limitation within the cathode leads to uneven utilization of cathode active materials across the coating thickness which in turn causes inhomogeneous CEI resistance growth across the electrode thickness. This generates a negative feedback loop that worsens the reaction inhomogeneity with each cycle, resulting in capacity fading.[15,16] Even in lithium iron phosphate (LFP)-based batteries, where CEI impedance remains stable because of its low voltage operation, thicker cathodes show faster capacity fade.[14] Li-ion conductivity (a product of total ionic conductivity and tt+) of most PEs are 1–2 orders of magnitude lower than liquid electrolytes, even at an elevated testing temperature (50–80 °C). Therefore, the diffusion-limitation-induced capacity fade will be expected at much smaller C-rates. Despite several reports on PE-SSBs, it is unclear to what extent the PE transport limitations also contribute to the dramatic capacity decay observed in $LiNi_xMn_yCo_{1-x-y}O_2$ (NMC)-based PE-SSBs. Most of the reports on PE-SSBs focus on mitigating the high-voltage stability issues at the CEI.[18–20]

Contact loss at electrolyte–electrode interfaces is an additional factor that can add to the capacity fade of PE-SSBs. To the authors' knowledge, this issue has not been well investigated in

---

[a] Oak Ridge National Laboratory, Chemical Sciences Division, Oak Ridge, TN 37831, USA. E-mail: ockj@ornl.gov; chenx@ornl.gov; sahorer@ornl.gov

[b] Oak Ridge National Laboratory, Computational Science and Engineering Division, Oak Ridge, TN 37831, USA

[c] Oak Ridge National Laboratory, Center for Nanoscale Materials Sciences, Oak Ridge, TN 37831, USA

[d] The Bredesen Center for Interdisciplinary Research and Graduate Education, The University of Tennessee Knoxville, Knoxville, TN 37996, USA

the literature for PE-SSBs. Altogether, cycling performance of a PE-SSB will be a complex function of the PE's (1) bulk ion-transport properties, (2) ion-transport properties of their interphase layers, (3) mechanical properties and interfacial adhesion with the electrodes, as well as (4) evolution of these properties with cycling, for a given anode–cathode combination. Diagnosing a cell's capacity fade requires systematic detangling of these various contributions, which has been missing for PE-SSBs. The development of cell platforms and analysis workflows to systematically evaluate the cell-level performance of various PEs can help inform materials development.

In this study, we (1) utilized a tunable SSB fabrication platform to systematically evaluate three types of PEs with widely different transport properties when paired with a high-voltage cathode (NMC622) and (2) quantitatively decoupled the contributions of kinetic limitations (concentration gradients and charge transfer reaction) towards capacity fade, from the IR growth induced capacity fade, which primarily stems from CEI impedance growth. Through a decoupling analysis, we demonstrate that the internal cell resistance growth rate does not necessarily correlate with the capacity fade rate; *i.e.*, the cell with the highest internal resistance did not show the fastest capacity decay. Kinetic limitations dominated the internal cell resistance in all the PEs investigated. The kinetic limitations, as defined here, originate from a combination of two factors: the high concentration gradient in the PE phase and slow charge transfer reactions at the NMC–catholyte interface. The former cannot be assessed by impedance spectroscopy, which typically employs small alternating current perturbations. No evidence of contact loss at the catholyte/cathode interface after cycling was found *via ex situ* scanning electron microscopy (SEM) and transmission electron microscopy (TEM) analyses. Unlike the bulk of related work in this field, which primarily focuses on improving the electrolyte's intrinsic properties, this work employs an in-depth cell-level analysis to reveal degradation mechanisms. The diagnosis methodology implemented herein can provide critical insights that will guide the future development of polymer electrolytes and electrolyte–electrode interfaces for next-generation solid-state batteries.

2. Results and discussion

2.1 Tunable cell platform for assembling PE-based SSBs

The cell making process is schematically illustrated in Fig. 1a. Crosslinkable liquid precursors of the PEs were drop-cast onto a standard slurry-cast, porous NMC622 ($LiNi_{0.6}Mn_{0.2}Co_{0.2}O_2$) electrode. A freestanding, pre-cured PE membrane disc of the same formulation was then placed on top. The entire stack was thermally cured to polymerize the infiltrated precursors within the cathode. The cured stack was assembled into a coin cell with a Li metal anode. This fabrication platform can be adapted to any crosslinkable PE while maintaining a consistent cathode microstructure.

Three different PEs with distinct ion-transport properties were investigated here: a crosslinked dual-ion conducting PE ('xPEO') with a t_+ of 0.05,[21] a crosslinked 'single-ion' conducting

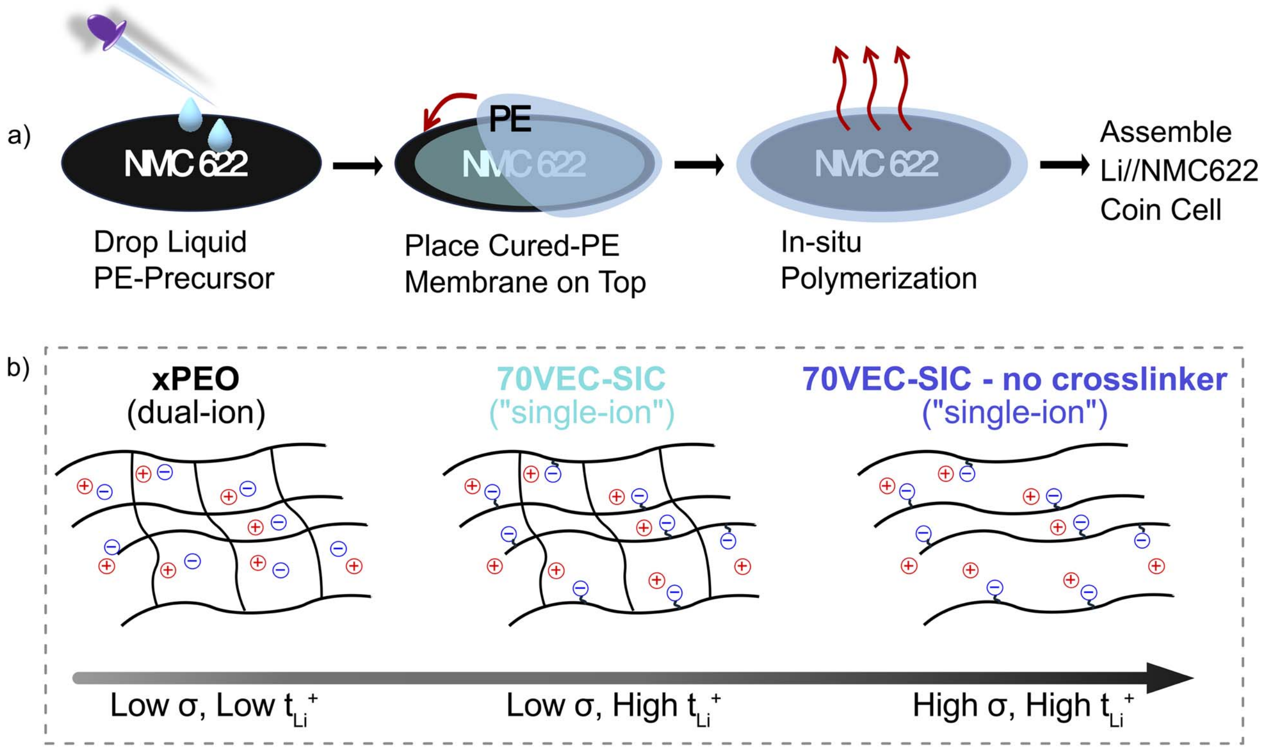

Fig. 1 (a) Schematic showing the infiltration procedure of a polymer electrolyte (PE) into a porous NMC622 cathode and (b) simplified polymer architectures of the three PEs utilized for this study. Li cations are shown as red circles, and anions (free or tethered to the polymer chains) are shown as blue circles. Polymer chains are shown as black lines.

Table 1 Ion transport properties of the three polymer electrolytes measured @70 °C

S. No.	Polymer electrolyte	Total conductivity (S cm^{-1})	Li^+ conductivity (S cm^{-1})	t_{Li^+}
1	xPEO	2.6×10^{-4}	1.3×10^{-5}	0.05
2	70VEC-SIC	3.1×10^{-5}	2.3×10^{-5}	0.75
3	70VEC-SIC – no crosslinker	1.4×10^{-3}	1.0×10^{-3}	0.75

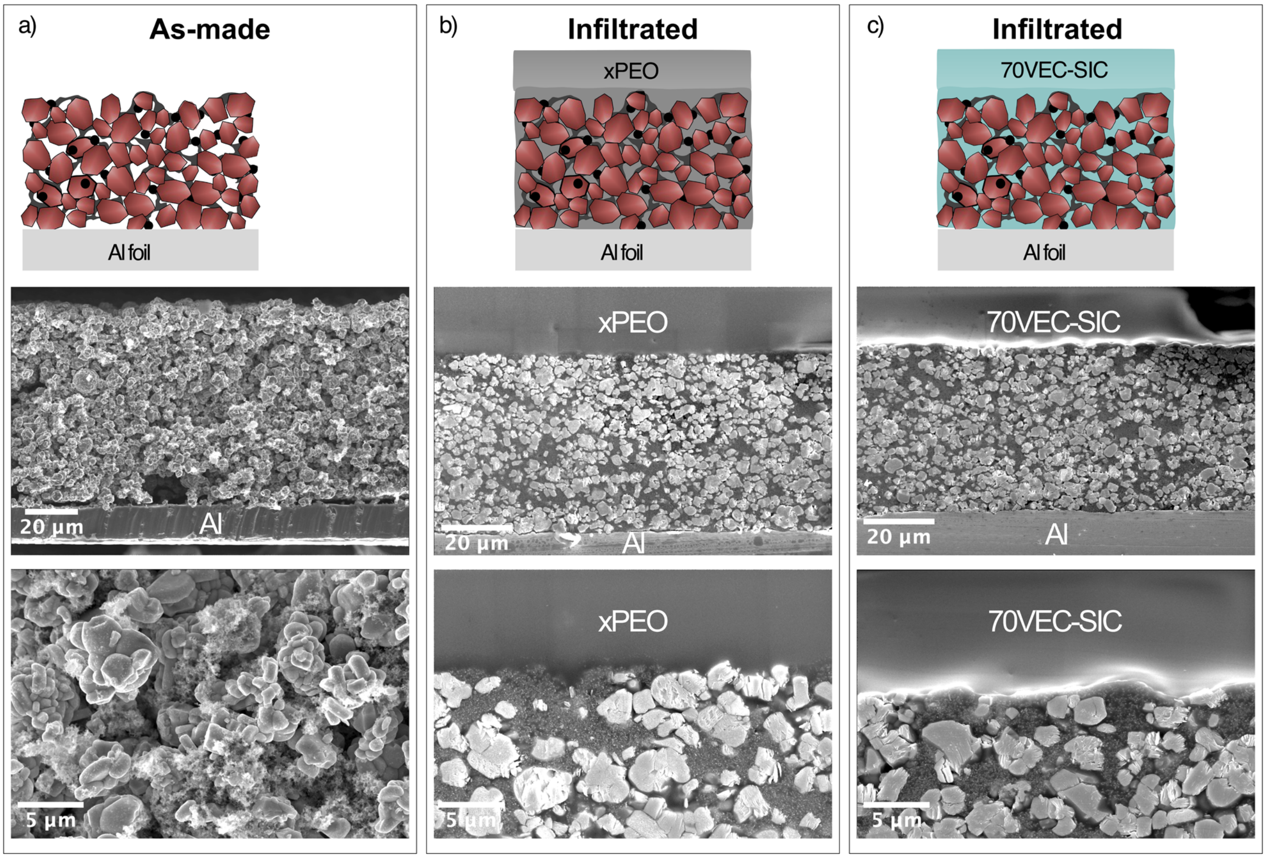

Fig. 2 Schematics and SEM images of the cross-sections of (a) an uncalendered, as-made cathode with PVDF binder, (b) a calendered cathode that was infiltrated with xPEO with a xPEO membrane on top, or alternatively, (c) infiltrated with 70VEC-SIC with a 70VEC-SIC membrane on top. All cross-sections were prepared using a cryomicrotome. Note that in the schematics in (b and c), the PE in the cathode *vs.* the PE membrane are shown in slightly different shades to emphasize the unfused/non-covalently bonded nature of this interface, even though the two PEs are identical in chemical composition.

PE ('70VEC-SIC') with a much higher t_+ of 0.75,[22] and the same single-ion PE without the crosslinker in the precursor solution ('70VEC-SIC – no crosslinker'). After curing, xPEO and 70VEC-SIC became solids, while 70VEC-SIC – no crosslinker resulted in a lower molecular weight viscous gel. Simplified polymer architectures of the PEs are schematically shown in Fig. 1b. In xPEO, both the Li cations and anions are untethered to the polymer chains and therefore mobile, resulting in its low tt+. For the other two PEs, the anions are covalently tethered to the polymer backbone. The immobilization of the anions promotes Li-ion selective motion, leading to a high tt+. The chemical structures of all precursor compounds are provided in Fig. S1. The ion transport properties of the three PEs, measured at 70 °C (same as the cycling temperature), are summarized in Table 1 and Fig. S2. xPEO had low t_+ and low Li^+ conductivity (total ionic conductivity multiplied by the t_+). 70VEC-SIC had low Li^+ conductivity but a high transference number. 70VEC-SIC – no crosslinker had both high Li^+ conductivity as well as high transference number.

To confirm infiltration of the PE precursors into the porous cathode after curing, cross-section SEM images were obtained (Fig. 2). Uninfiltrated cathode's cross-section shows the typical microstructure of a slurry-cast electrode, where NMC622 particles are loosely connected *via* a carbon black and PVDF network, to generate significant porosity (Fig. 2a). The as-made cathodes were calendered prior to infiltration to reduce thickness and facilitate ion transport within the composite cathode.[23] Complete infiltration occurred throughout the cathode

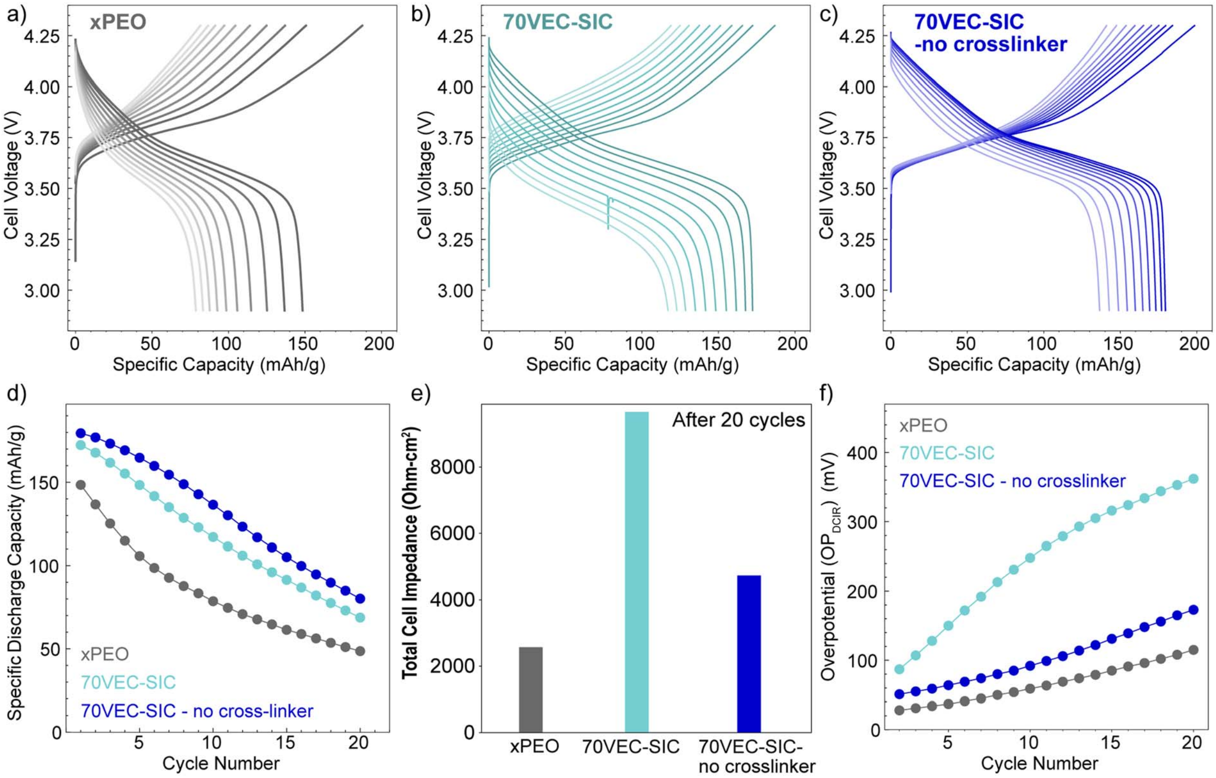

Fig. 3 (a–c) Charge/discharge voltage profiles of the first 10 cycles of the three PE types cycled at 50 μA cm^{-2} and 70 °C. (d) Specific discharge capacity *vs.* cycle number. (e) Total cell impedance after 20 cycles, measured *via* EIS. (f) IR drop overpotentials (OP$_{\mathrm{DCIR}}$) measured from voltage profiles at the beginning of charge steps over 20 cycles.

thickness (Fig. 2b, c and S3). The 70VEC-SIC-infiltrated cathode is microstructurally similar to the xPEO-infiltrated cathode. A seamless interface of the composite cathode with the free-standing PE membrane can also be seen. This is likely due to the presence of a thin layer of excessive PE at the cathode surface after infiltration. Such seamless contact with the PE membrane not only facilitates efficient ion transport across the cell but also improves electrolyte/electrode interfacial adhesion, which is necessary for achieving reversibility in PE-SSBs.[24]

2.2 Quantitative analysis of capacity fade drivers

Using this cell fabrication method, three types of Li||NMC622 coin-cells were assembled corresponding to the three PE catholyte types (‘xPEO’, ‘70VEC-SIC’, and ‘70VEC-SIC – no cross-linker’). In each cell, the catholyte and separator PEs were of the same formulation, except for the cell with the 70VEC-SIC – no crosslinker catholyte, where 70VEC-SIC was used as the separator. All cells underwent 20 charge/discharge cycles between 4.3 and 2.9 V *vs.* Li/Li$^+$ at 50 μA cm^{-2} and 70 °C. Fig. 3a–c show charge/discharge voltage profiles of each cell type's first 10 cycles. Specific discharge capacity (DC) *vs.* cycle number is compared in Fig. 3d. Repeat data obtained for one of the cell types showed good reproducibility of the capacity fade rate (Fig. S4). For the same cathode active material (NMC622), a large variability in both the achievable discharge capacity (DC) and capacity fade rate can be seen depending on the PE type. The 70VEC-SIC – no crosslinker catholyte, which has the best transport properties (high t_+ and high Li$^+$ conductivity), outperformed the other two catholytes in both achievable DC and capacity retention. The xPEO catholyte, which has the worst transport properties, showed the lowest achievable DC and capacity retention. This indicates the role of the PEs' ion transport properties in determining the capacity fade in these cells. Interestingly, despite the similar Li$^+$ conductivities of xPEO and 70VEC-SIC, a large difference in both achievable capacity and capacity fade was observed between the two.

To understand capacity fade, internal resistance growth of the three cells was first compared. Electrochemical impedance spectroscopy (EIS) was conducted before and after 20 cycles, in the discharged state. As expected, cell impedance grew in all three cells after 20 cycles (Fig. S5). The total cell impedance for the three cell types after 20 cycles is compared in Fig. 3e. The highest impedance growth was observed for the 70VEC-SIC cell, followed by 70VEC-SIC – no crosslinker and xPEO cells. This is consistent with the growth rates of IR drop overpotentials (OP$_{\mathrm{DCIR}}$) observed in the three cells (observed at the beginning of a charge/discharge voltage profile as a step-like feature and a measure of the cell's direct current internal resistance (DCIR)) (Fig. 3f). The difference in the impedance trend compared to the capacity fade trend suggested that while the impedance growth likely contributed to the overall capacity fade, the internal cell resistance alone does not explain observed capacity fade trends. Additional factors – such as kinetic limitations (defined

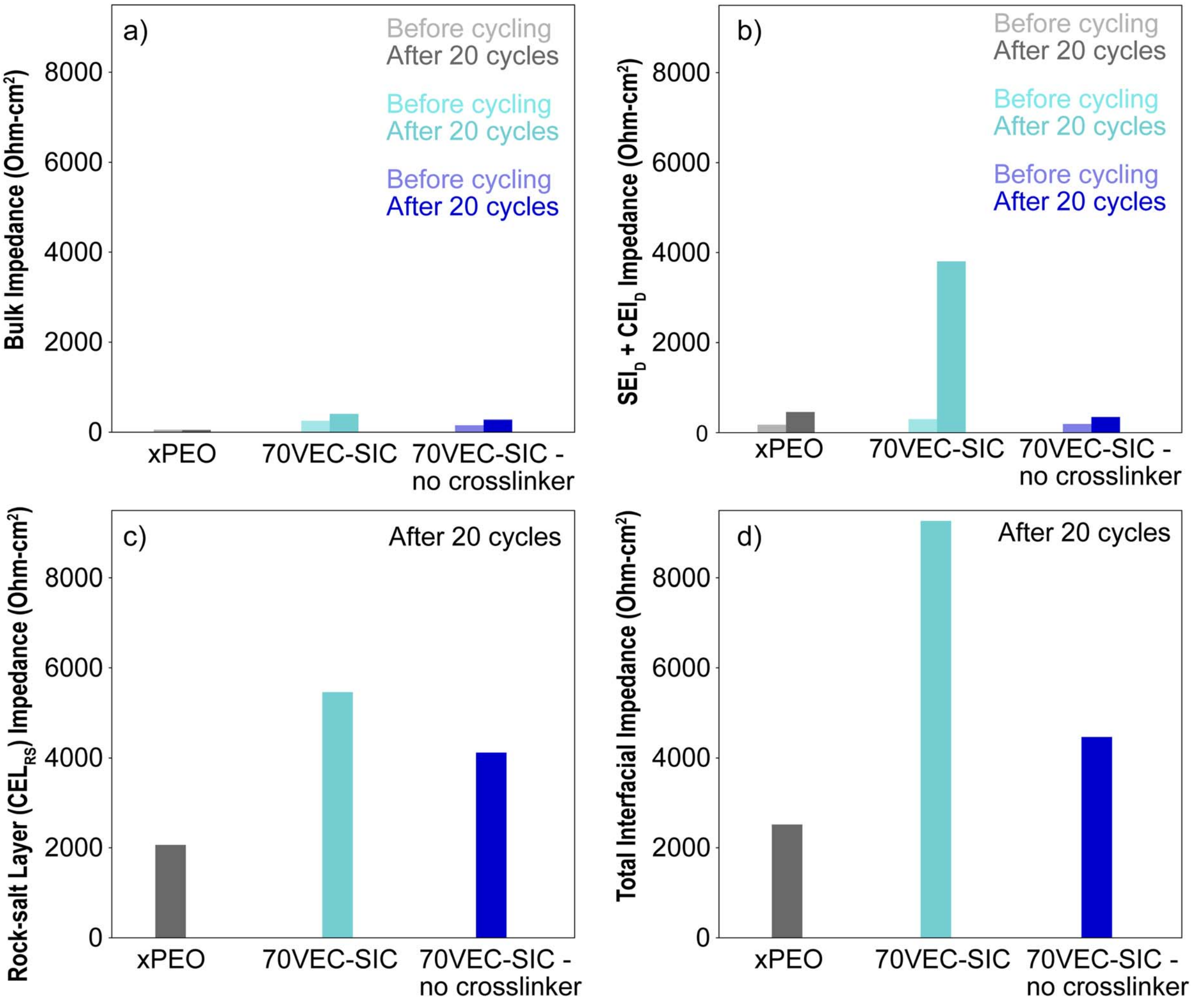

Fig. 4 Breakdown analysis of EIS Nyquist plots of Li||NMC622 cells made with the three types of PEs: 'xPEO', '70VEC-SIC', and '70VEC-SIC – no crosslinker' into (a) bulk impedance, (b) SEI_D + CEI_D impedance, and (c) rock-salt layer's impedance (CEI_{RS}). (d) Total interfacial impedance, calculated by adding (b) and (c) values. The "before cycling" data were obtained at 70 °C before the start of cycling, and the "after cycling" data were obtained after 20 cycles at 50 μA cm^{-2} and 70 °C and after discharging to 2.9 V *vs.* Li/Li$^+$.

previously) – are playing an unignorable role towards capacity fade in these cells. Then, the question becomes – how can we quantify the contribution of each factor towards capacity fade? The method to decouple these contributing factors will be introduced shortly after a breakdown analysis of the total cell impedance.

To identify the source/s of impedance growth, the total cell impedance was broken into three components (Fig. 4 and Table 2): (1) bulk ion-transport impedance, assigned primarily to the ionic conductivity of the PE phase (separator + catholyte) as measured under small alternating current perturbations, (2) total ion-transport impedance of the PE decomposition layers at the electrode interfaces (SEI_D + CEI_D), assumed to be of ohmic character, and (3) impedance of the rock-salt layer formed at the surface of cathode particles during cycling (CEI_{RS}) (a non-ohmic diffusion resistance and dependent on cathode's state-of-charge (SOC)), coupled with charge transfer impedance at the CEI (Butler–Volmer rate law; a non-ohmic component).[25] The bulk impedance growth of the PE phase was small in all cells and grew in insignificant amounts compared to total cell impedance (Fig. 4a). The combined SEI_D + CEI_D impedance grew significantly only for the '70VEC-SIC' cells (Fig. 4b). However, the largest contribution to the total cell impedance in all cases originated from the restructured rock-salt layer at the NMC622 surface (CEI_{RS}) (Fig. 4c). The total interfacial impedance (SEI_D + CEI_D + CEI_{RS}) was therefore highest for 70VEC-SIC cells (Fig. 4d), consistent with the highest contributions of OP_{DCIR} for these cells. For xPEO and 70VEC-SIC – no crosslinker cells, the total interfacial impedance was smaller, although still in the range of multiple 1000s of Ω cm^2. Further EIS analysis details can be found in Note S1, Fig. S6.

To quantitatively determine the relative contributions of the two capacity fade drivers, a methodology proposed by Zhang *et al.*[26] for failure analysis of liquid electrolyte-based Li metal cells was adapted here. This method involves decoupling the various OPs present in a charge/discharge voltage profile by comparing it with a thermodynamic reference voltage profile of the same cathode. Herein, a Li||NMC622 cell made with

Table 2 Circuit parameter fits of all six cells' EIS spectra, obtained before cycling and after 20 cycles (NA = not applicable). The area of cathode is 0.97 cm^2

	PE bulk (Ohm)	$\mathrm{SEI_D}$ + $\mathrm{CEI_D}$ (Ohm)	Rock-salt layer ($\mathrm{CEI_{RS}}$) (Ohm)	Total interfacial impedance (Ohm)	Total cell impedance (Ohm)	Frequency range (bulk, $\mathrm{SEI_D}$ + $\mathrm{CEI_D}$, and rock-salt layer ($\mathrm{CEI_{RS}}$))
xPEO (before)	56	175	NA			>200 kHz, 200 kHz–2 Hz, and <2 Hz
xPEO (after)	52	454	2064*	2518	2570	>200 kHz, 200 kHz–1 Hz, and <1 Hz
70VEC-SIC (before)	254	292	NA			>6 kHz, 5 kHz–1 Hz, and <1 Hz
70VEC-SIC (after)	402	3808	5458	9266	9668	>15 kHz, 15 kHz–1 Hz, and <1 Hz
70VEC-SIC – no crosslinker (before)	154	193	NA			>30 kHz, 30 kHz–3 Hz, and <3 Hz
70VEC-SIC – no crosslinker (after)	275	340	4119*	4459	4734	>7.5 kHz, 7.5 kHz–1 Hz, and <1 Hz

a standard liquid electrolyte and cycled @$\sim$C/100, 70 °C was used as the near-thermodynamic reference because of minimal kinetic barriers expected under these cycling conditions. The analysis method can be broken into three steps (Fig. S7). First, the IR potential drop ($\mathrm{OP_{DCIR}}$) is noted from the charge/discharge voltage profile (Fig. S7a). This OP origination primarily corresponds to the total cell impedance (PE bulk impedance + $\mathrm{SEI_D}$ + $\mathrm{CEI_D}$ + $\mathrm{CEI_{RS}}$ impedance (SOC dependent; coupled with charge-transfer impedance). Second, $\mathrm{OP_{DCIR}}$ is subtracted from the entire corresponding charge/discharge voltage profiles (Fig. S7b). Third, the after-subtraction voltage profile is shifted along the *x*-axis (capacity), such that the starting cell voltage lies on the thermodynamic reference voltage profile (Fig. S7c). After this step, deviation of the cell voltage profile w.r.t. the reference profile is noted. These additional OPs primarily stem from concentration gradients within the PE phase (referred to as $\mathrm{OP_{PE}}$), coupled with their impact of the charge-transfer reaction impedance at the CEI ($\mathrm{OP_{CT}}$). We bundle these two kinetic OPs as '$\mathrm{OP_{PE+CT}}$'. The $\mathrm{Li^+}$ concentration gradients are generated within the PE phase due to their less than unity t_+.[27,28] Thus, PE's $\mathrm{Li^+}$ concentration will change at the particle surface as the cycle progresses, depending on the severity of $\mathrm{Li^+}$ concentration gradients. In the cathode, the bulk $\mathrm{Li^+}$ diffusivity of NMCs decreases dramatically near the high depth of discharge (DOD) after being roughly constant over the rest of the SOC.[29,30] This would decrease the charge transfer reaction rates near the high DOD. Altogether, these changes with the passage of direct current (charge/discharge) will impact the $\mathrm{OP_{PE+CT}}$.

Thus, this analysis method decouples the kinetic limitation-induced OPs ($\mathrm{OP_{PE+CT}}$) from the $\mathrm{OP_{DCIR}}$. This in turn can be used to quantify their individual contributions to capacity loss (discussed next in Fig. 5). The effect of internal cell resistance ($\mathrm{OP_{DCIR}}$) on the cathode's true state-of-charge at the beginning of a charge/discharge step and the corresponding capacity loss is shaded in blue in Fig. 5d–f. More importantly, the effect $\mathrm{OP_{PE+CT}}$ or kinetic limitation-induced capacity loss as the cell is charged/discharged is shaded in orange in Fig. 5d–f.

Fig. 5a–f show the unprocessed and processed voltage profiles of first 5 cycles. Reference cell's five cycles are shown in red. After data processing, removal of the $\mathrm{OP_{DCIR}}$ caused the voltage profiles of the '70VEC-SIC – no crosslinker' cell to nearly overlap with the reference, with the least amount of $\mathrm{OP_{PE+CT}}$. Similarly, the processed voltage profile was significantly closer to the reference profile in the '70VEC-SIC' cell, although relatively higher $\mathrm{OP_{PE+CT}}$ were observed. In contrast, in the 'xPEO' cell, large $\mathrm{OP_{PE+CT}}$ remained throughout the discharge step. Each cycle's cumulative discharge capacity loss was broken into two components corresponding to the two types of OPs described above. Component 1: $\mathrm{OP_{DCIR}}$ growth-driven capacity loss; Component 2: $\mathrm{OP_{PE+CT}}$ growth-driven capacity loss. The former was obtained by reading the specific capacity value at the start of each processed profile (highlighted for the 5th discharge *via* a blue shaded box). The latter was obtained by reading the specific capacity at the end of each processed profile, followed by subtracting this value from the reference cell's near-theoretical discharged capacity (highlighted for the 5th discharge *via* orange shaded boxes). Altogether, these two constituted 100% of capacity loss in our analysis. The growth of these components determined the capacity fade rate.

The contribution of $\mathrm{OP_{DCIR}}$ growth and $\mathrm{OP_{PE+CT}}$ growth to capacity fade is quantified by the bar charts shown in Fig. 5g–i. For the xPEO cell, $\mathrm{OP_{PE+CT}}$ growth-driven capacity loss was at least a factor of two larger than the two 70VEC-SIC cells. For the crosslinked 70VEC-SIC cell, a significant source of capacity fade was its $\mathrm{OP_{DCIR}}$ growth. At cycle 5, the growth of $\mathrm{OP_{DCIR}}$ accounted for nearly 40% of its total capacity loss. For the 70VEC-SIC – no crosslinker cell, $\mathrm{OP_{DCIR}}$ was the smallest amongst the three cells; however, its $\mathrm{OP_{PE+CT}}$ was not significantly different from that of the crosslinked 70VEC-SIC cell.

We highlight two observations from the decoupling analysis: first, despite the similar $\mathrm{Li^+}$ conductivities of the 'xPEO' and '70VEC-SIC' PEs (1.3×10^{-5} S cm^{-1} and 2.3×10^{-5} S cm^{-1}, respectively), their $\mathrm{OP_{PE+CT}}$ were significantly different. In other words, although EIS-measured static bulk resistances are similar between these two catholytes, their kinetic limitations are vastly different. The $\mathrm{OP_{PE}}$ of the xPEO cell is expected to be significantly larger than the $\mathrm{OP_{PE}}$ of the 70VEC-SIC cell, due to its much smaller transference number (0.05 *vs.* 0.75). To confirm the presence of $\mathrm{OP_{PE}}$ under the mild cycling conditions employed here (70 °C and $\sim$C/50), numerical simulations were performed using the actual electrolyte, cell, and cycling parameters (complete details are provided in the Experimental section). Briefly, the NMC622 single crystal particles were

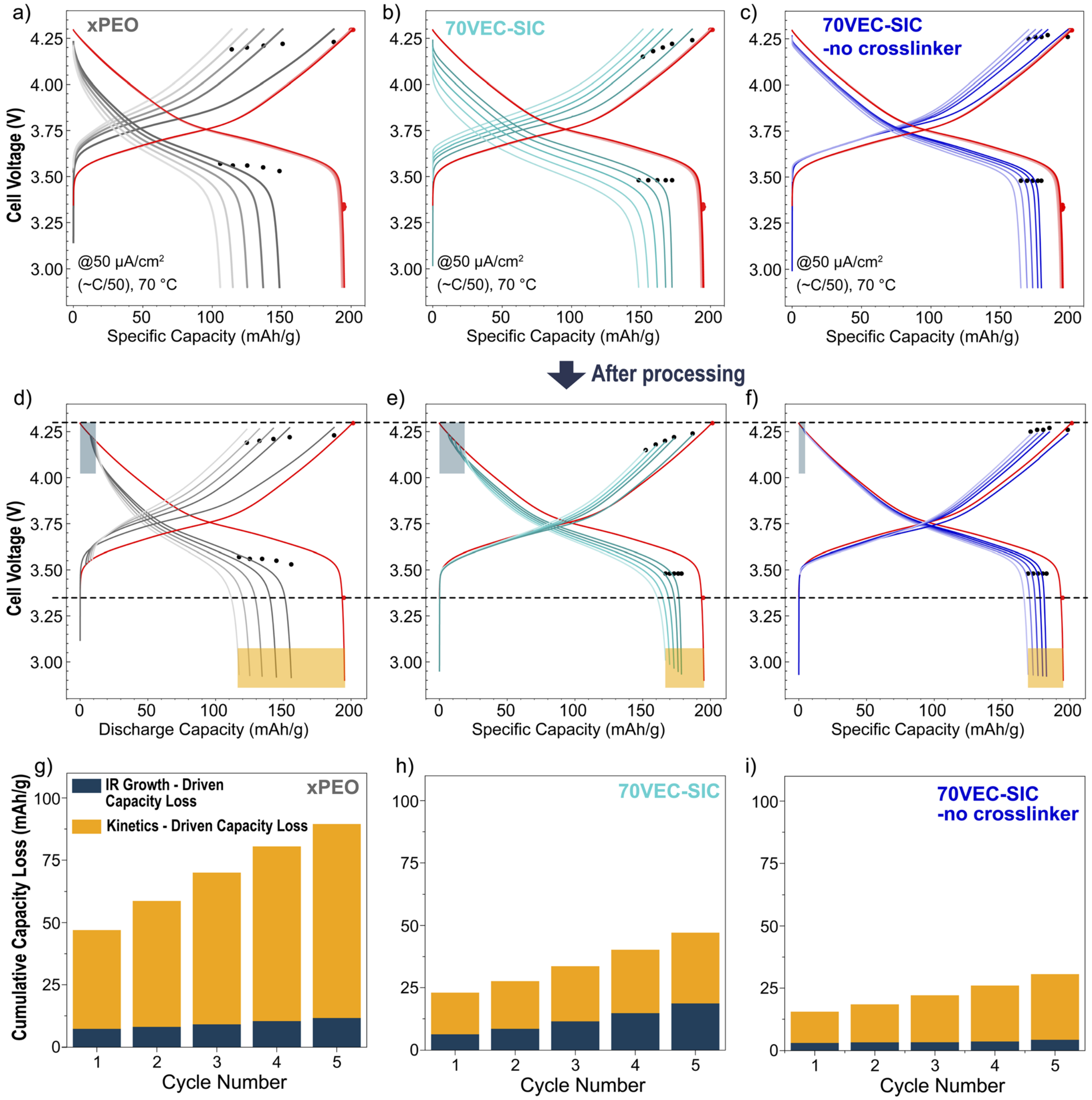

Fig. 5 (a–c) Charge/discharge voltage profiles of the three types of cells ('xPEO', '70VEC-SIC', and '70VEC-SIC – no crosslinker'), obtained for the first 5 cycles (50 μA cm^{-2} and 70 °C). A comparison with a reference cell made with a liquid electrolyte and cycled @ ~C/100 is included to get a close to thermodynamic voltage profile (5 cycles are shown). Dots correspond to the cells' OCV values obtained after 1-hour of rest following each charge/discharge. (d–f) The voltage profiles shown in (a–c) after processing (only the first cycle of the liquid reference cell is shown). The dashed lines are included to highlight the deviations of OCV as a function of cell type and cycle number w.r.t. the reference cell. Blue and orange shaded regions correspond to the blue and orange portions of the bar graph in (g–i), respectively. (g–i) Bar graphs showing the breakdown of capacity loss observed in each of the five cycles into IR-growth-driven capacity loss and kinetic limitation-driven capacity loss for the three cell types.

approximated in 2D as rectangles with the particle size and aspect ratio distribution representing the actual cathode. The NMC electrode was taken to be 50 μm thick to match the actual electrode's thickness. The NMC particles were surrounded by a porous binder/carbon black foam filled with the PE and thus capable of conducting both electrons and ions. The rest of the geometry was represented by an 80 μm thick layer of PE (again close to the actual cell separator thicknesses), and the counter electrode was modeled as a Li electrode surface. An equivalent of the current density used in the experiments, 32 μA cm^{-2}, was applied to the current collector surface, and the cell charging was simulated until 4.3 V as a stop condition. The results after a single charge to 4.3 V *vs.* Li/Li$^+$ are shown in Fig. 6. As expected, the highest concentration gradient built up in the PE phase was observed in the xPEO cell, resulting in a significantly larger NMC particle's Li$^+$ concentration (*i.e.* smaller achievable

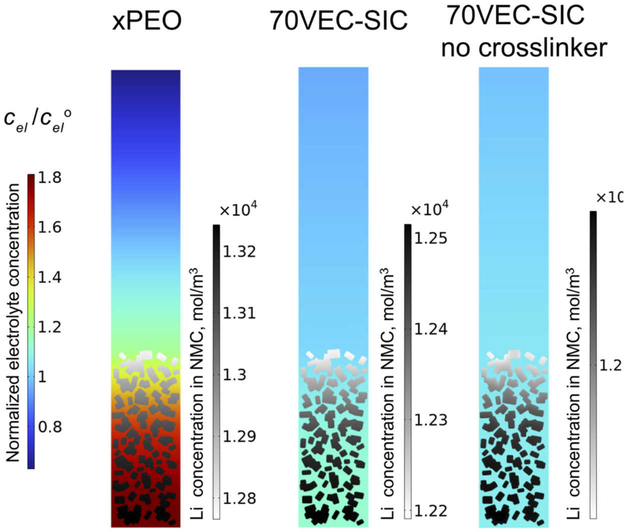

Fig. 6 Simulated concentration of Li^+ in the PE phase, and the cathode active material after charging to 4.3 V *vs.* Li/Li^+ under 32 μA cm^{-2} current. The scale for the electrolyte concentration (normalized to the initial concentration) is kept the same for both scenarios. The concentration of Li in NMC is represented by individual scales for each simulation.

charge capacity) compared to the two 70VEC-SIC cells. Note that, for simplicity, the charge transfer impedance at the CEI was assumed to be zero, and the SOC-dependence of NMC's bulk Li^+ diffusivity was omitted. Overall, these results imply that t_+ is playing an important role in not only the achievable capacity[31,32] but also the capacity retention of PE-SSBs. The OP_{PE} is not reflected in the static impedance measurements. This is why internal cell resistance did not predict the capacity fade rate. Decoupling analysis introduced in this work effectively revealed the impact of bulk ion transport properties of the PE catholyte on cumulative capacity fade.

Second, we observed that although Li^+ conductivity for '70VEC-SIC – no crosslinker' was 1.0×10^{-3} S cm^{-1}, close to 2 orders of magnitude higher than that for '70VEC-SIC' (2.3×10^{-5} S cm^{-1}), yet after removal of OP_{DCIR}, their OP_{PE+CT} was not significantly different. For these cells with high t_+ PEs, OP_{PE} is relatively small, according to the numerical simulations shown in Fig. 5. Therefore, OP_{CT} growth was likely the main contributor to capacity fade. This point is strengthened by Fig. 7, where we tested a Li‖LFP cell that was prepared using the infiltration method with 70VEC-SIC – no crosslinker PE. LFP as a low-voltage cathode does not form a rock-salt layer during cycling, and PE decomposition is not expected. Indeed, the cell impedance remained very stable during cycling (Fig. S8). The cell was cycled at increasing current densities, with 5 cycles at each current density. As can be seen, the cell showed no capacity fade over the first 15 cycles. In the LFP cell, both OP_{PE} and OP_{CT} were small and stable. The LFP results combined with numerical simulations strongly suggest that a growing OP_{CT} was the main driver for capacity fade in the two 70VEC-SIC NMC cells.

Note that the impact of the Li anode on capacity fade was deemed not a significant factor and was excluded in this analysis for the following reasons: (1) the use of 600 μm thick Li anodes avoided Li inventory loss. (2) High temperatures (70 °C) and low currents utilized for cycling improved the contact at the anode interface and minimized Li loss due to voiding. (3) The relatively small role of the Li anode in capacity fade in the initial cycles of Li|PE|NMC622 cells was shown in our recent work.[33]

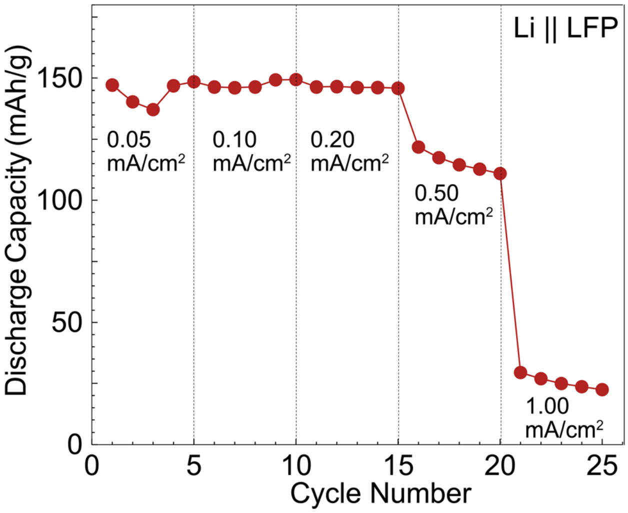

Fig. 7 Specific discharge capacity *vs.* cycle number of a Li‖LFP cell made *via* the same infiltration method as Fig. 1, using 70VEC-SIC – no crosslinker PE. Discharge current was increased every 5 cycles, while the charge current was fixed at 0.05 mA cm^{-2}. Cycling occurred at 70 °C.

2.3 Characterization of the cathode/PE interface after cycling

The cycled NMC622|PE interface as well as the bulk PE phase were further examined using cryo-STEM (Fig. 8). Thin sections (∼100 nm thick) of the NMC|PE cell stack (minus the Li anode) were prepared using a cryo-microtome. Core-loss electron energy-loss spectroscopy (EELS) mapping was performed at the NMC|PE interface as well as in the bulk PE region. The oxygen bonding environment as a function of distance from the cathode particle surface was analyzed. Profiles averaging the oxygen K-edge signal along the particle surfaces were generated, and representative EELS spectra (color-coded to correspond to the colors of the surface profiles) are shown in Fig. 8a and b. To prevent significant decomposition of the PE structure due to electron beam damage, the electron dose applied was set to ∼2 $\times 10^2$ e^- $Å^{-2}$, which limited the spatial resolution of these measurements to ∼20 nm. Going from the PE phase to the NMC622 phase, the O K-edge changed from one prominent peak at 537 eV and a broad peak to two prominent peaks, labeled P1 and P2. These are the representative peaks seen in pristine NMC particles.[34] The P1 peak corresponds to O 1s excitations to unoccupied hybridized transition metal 3d/oxygen 2p states.[35] Importantly, the rock-salt layer typically features a significantly decreased P1 peak intensity.[34] In Fig. 8c, we show the P1 peak intensity fraction as a function of distance from the interface, for both xPEO and 70VEC-SIC cells. We found the thickness of the O-deficient rock-salt layer at the NMC

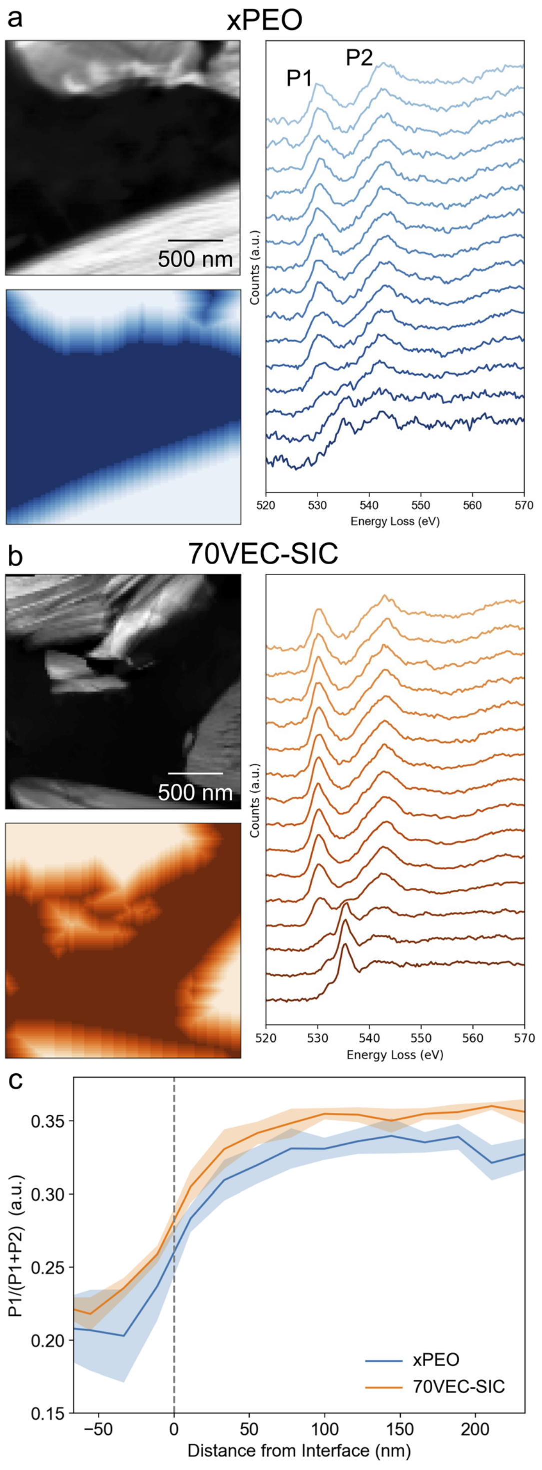

Fig. 8 Cryo-STEM EELS oxygen bonding environment and cathode particle surface profile analysis of xPEO and 70VEC-SIC cells. (a) Annular dark-field (ADF) image of NMC622|xPEO interfaces (top left), surface profiles (bottom left), and corresponding averaged O K-edge spectra (right). (b) ADF image of NMC622|70VEC-SIC interfaces (top left), surface profiles (bottom left), and corresponding averaged O K-edge spectra (right). (a and b) The colors of the EELS spectra correspond to the colors of the surface profiles. (c) Average intensity of the P1 peak (O 1s to TM 3d/O 2p excitations) normalized to integrated intensities of P1 and P2. It shows decreased P1 intensity near the particle surfaces, consistent with a rock-salt layer, and little difference between the cells on the scale of tens of nanometers.

surface to be similar in these two samples, within the resolution of EELS mapping. We note that extreme beam sensitivity of the PE phase was still present even under such mild imaging conditions (cryotemperature + low dose); therefore, beam modifications of local bonding environments were not totally avoided, and this may also have obscured differences in the rock-salt layer thickness at very small scales. Given the significant CEI impedance growth observed from EIS analysis, we suggest that the rock-salt layers may be present but thinner than 20 nm. This thickness range is reasonable, as for NMC cathodes cycled with liquid electrolytes, this high-impedance layer is typically detected to be <20 nm.[34,36]

The PE decomposition layer thickness was not determined using this method due to the PE phase's beam sensitivity. The O K-edge spectra of the PE phase near the interface and those in the bulk PE separator region did not show differences. However, at least one of the two PEs (xPEO) is known to decompose when operated in NMC622 cathodes. Beam-induced modification of the PE phase may have wiped out the differences between the PE decomposition layer and the bulk. Another possibility is that the thickness of the PE decomposition layer is also very small, <20 nm.

Little physical contact loss at the NMC622|PE interface was observed in any of the cycled cathode datasets (data not shown) and that it may have been due to the ultramicrotomy preparation. Cross-sectional SEM images (Fig. S9) also suggest the absence of any significant contact-loss issue in these cells. Intraparticle cracking is also not expected in these cells because of the use of single-crystalline NMC622 particles.[37–39] Therefore, these effects were considered minimal when explaining the capacity fade trends.

Broadly, the results obtained here demonstrate that even at an elevated cycling temperature (70 °C) and a low cycling current density (50 μA cm^{-2} or ∼C/50) (both of which should alleviate transport limitations), significant ion-transport limitations are still at play in impacting the capacity fade of these cells. These limitations are expected to worsen at room temperature and will be dictated by their PE-specific drops in ionic conductivity and transference number. Similarly, at higher cycling currents, all the ohmic overpotentials will increase linearly in proportion to the current increase, while the non-ohmic overpotentials will increase non-linearly according to their individual current-dependence relationships.

3. Conclusions

We conducted a quantitative analysis of the capacity fade of polymer electrolyte (PE)-based solid-state batteries (SSBs) containing a high-voltage NMC cathode by decoupling their primary capacity fade contributors: cell's internal resistance growth (primarily from the cathode electrolyte interface (CEI)) and kinetic limitations stemming from the high concentration gradient in the catholyte and slow charge transfer reactions at the cathode particle–PE interface. A modular cell-fabrication platform to assemble PE-based SSBs was developed, involving infiltration and curing of solvent-free polymer electrolyte (PE) precursors. This platform was utilized to independently change the PE type while keeping the remaining cell aspects the same – an easy task with liquid-electrolyte-based batteries, but non-trivial with SSBs. Three different PE types were compared: a low ionic conductivity and low t_+ PE, xPEO, a low ionic conductivity and high t_+ PE, 70VEC-SIC, and a high ionic conductivity and high t_+ PE, 70VEC-SIC – no crosslinker.

A voltage profile analysis methodology was utilized to distinguish and quantify the two types of capacity fade drivers – cell's internal impedance induced overpotential, OP_{DCIR}, and kinetic limitation induced overpotential, OP_{PE+CT}. OP_{DCIR} growth induced capacity fade correlates well with the cell's internal impedance growth, with cathode interfacial impedance as its main contributor. OP_{DCIR} is the largest and grew the fastest in the 70VEC-SIC cell. However, this cell did not show the highest capacity fade rate. OP_{PE+CT} dominated the capacity fade. The xPEO cell, whose OP_{PE} was the largest (lowest t_+), had the fastest capacity fade, demonstrating the importance of t_+ towards capacity fade. In other words, the concentration gradient induced kinetic limitations are not reflected in the static impedance measurements, and thus these alone cannot predict capacity fade. The methodology presented here effectively revealed the impact of catholyte's ion transport properties on capacity fade. A comparison with a similar PE-SSB employing an LFP cathode confirms that the adverse impact of transport limitations on the capacity fade of NMC-based cells is amplified by their high CEI impedance growth.

Cryo-STEM-EELS analyses indicate the thickness of the rock-salt layer as well as any PE decomposition layer at the CEI to be less than 20 nm thick, for both xPEO and 70VEC-SIC cells. The impact of any contact loss at the PE|NMC622 interface was excluded in this study's capacity fade analysis as it was not observed by both TEM and SEM.

4. Experimental section

4.1 Materials

Vinyl ethylene carbonate (VEC, Sigma-Aldrich) was dried over molecular sieves. Lithium bis(trifluoromethanesulfonyl)imide (LiSTFSI, SPECIFIC POLYMERS) was used as received. Azobisisobutyronitrile (AIBN, Sigma-Aldrich) was recrystallized. Polyethylene glycol dimethacrylate (PEGDMA, average Mn: 1000, Polysciences) was used as received. Poly(ethylene glycol) diglycidyl ether (PEGDGE, average Mn: 500, Sigma-Aldrich) was used as received. All these chemicals are temperature-sensitive and were therefore stored in a refrigerator after sealing the individual containers in an argon glovebox with Parafilm tape. *O*,*O*′-Bis(2-aminopropyl) polypropylene glycol-*block*-polyethylene glycol-*block*-polypropylene glycol (Jeffamine ED-2003, Huntsman Corporation) was used as received. Lithium bis(trifluoromethane)sulfonimide (LiTFSI, 3 M) was dried under vacuum at 120 °C for 3 days and stored inside an argon glovebox.

4.2 Preparation of polymer electrolytes

The compositions and the preparation methods of the 70VEC-SIC and xPEO polymer electrolytes (PEs) were the same as reported before.[21,22] To prepare the single-ion conducing PE (70VEC-SIC), LiSTFSI, PEGDMA, VEC and AIBN were stirred in an argon glovebox until fully dissolved. The weight ratio of VEC to PEGDMA was fixed at 7 : 3. The prepared solution was poured between two glass plates, separated by cover glass slips, then cured at 80 °C for 1 hour. The resulting transparent 70VEC-SIC membrane was punched into 5/8″ discs and stored in the argon glovebox without additional drying. To prepare the dual-ion conducting PE (xPEO), Jeffamine ED2003, PEGDGE and LiTFSI were stirred in isopropyl alcohol (IPA, Sigma-Aldrich) at 40 °C in air until fully dissolved. IPA was then removed using a rotary evaporator. The resulting solution was poured and blade-cast onto a Mylar substrate, followed by drying at 60 °C for 2 h, and subsequently curing at 100 °C for 12 h. Finally, the membrane was peeled off, punched into 5/8″ discs, further dried in a vacuum oven at 100 °C for 12 h, and stored in an argon glove box.

4.3 Cathode preparation

All cathodes were prepared inside an argon glove box. For the polyvinylidene fluoride (PVDF)-based cathodes, the NMC622 single crystal (Targray, 89 wt%) cathode, carbon black (Super C65 from Timcal, 5 wt%) as a carbon additive, and PVDF (KYNAR® POWERFLEX LBG powder, Arkema High Performance Polymers, 6 wt%) as a binder were mixed using an agate mortar and dispersed in *N*-methylpyrrolidone solvent to prepare a slurry. The obtained slurry was blade-cast on a carbon-coated Al current collector and dried at 100 °C for over 2 h. Subsequently, the cathode sheet was calendered, punched into 7/16″ discs, and vacuum dried at 120 °C overnight. The typical mass loading of NMC622 on the Al foil was 13 mg cm^{-2}.

4.4 Cell assembly

2032-type coin cells were assembled inside an argon-filled glove box in two different cell designs focusing on the cathode/electrolyte interfaces. In all the cells, a freestanding PE membrane of the same formulation as in the composite cathode was placed on top of the cathode, followed by a Li anode (600 μm thick, MTI Corp.). For the infiltrated cells, prior to coin cell assembly, a PE-integrated cathode was first prepared using an *in situ* polymerization method. A punched cathode (PVDF-based) disc was placed on a stainless-steel spacer. Then, a droplet of the PE precursor mixture was spread onto the cathode. Subsequently, it was covered with a freestanding polymer membrane and *in situ* polymerized at the designated temperature (80 °C for 70VEC-SIC and 100 °C for xPEO). The electrolyte-integrated cathode, PE membrane, and Li metal were assembled into coin cells. The specific capacity was calculated based on mass loading of NMC622 in the composite cathode.

4.5 Electrochemical testing

Galvanostatic charge/discharge measurements on Li//NMC622 cells were conducted using an electrochemical analyzer (VSP-3e, BioLogic) at 70 °C. All the cells were equilibrated at 70 °C for 2 days before cycling. The cut-off potentials were set at 4.3–2.9 V. In the cycling test, the charge current density was fixed at

$0.05\ \mathrm{mA\ cm^{-2}}$. The electrochemical impedance spectra (EIS) of cells were collected in the frequency range of 1 MHz to 0.1 Hz at a voltage amplitude of 6 mV, after 2 days of conditioning (before cycling) and after the 20th discharge.

For the ionic conductivity measurements, xPEO and 70VEC-SIC membranes were sandwiched between two stainless steel electrodes, and EIS measurements were conducted in a temperature range from −20 °C to 80 °C using a temperature-controlled chamber (SU-222, ESPEC) in the frequency range from 7 MHz to 0.1 Hz with a voltage amplitude of 6 mV. The uncrosslinked 70VEC-SIC was measured in a custom-made liquid cell containing two parallel stainless steel disks (10.2 mm in diameter each) and separated by 0.3 mm.

The Li-ion transference number (tt+) was determined using the Bruce–Vincent method under anion-blocking conditions.[40,41] A Li symmetric cell was assembled with the xPEO or 70VEC-SIC membrane sandwiched between two Li electrodes. The uncrosslinked 70VEC-SIC was templated by two stacked Mylar washers (outer diameter: 5/8″; inner diameter: 7/16″; thickness ~100 μm) in between the Li electrodes to ensure containment.

4.6 NMR measurements

NMR spectra and diffusion data were recorded using a Bruker Avance Neo 400 MHz narrow bore spectrometer equipped with a high gradient ^{1}H/X diffusion probe (Bruker Diff50). All NMR measurements were conducted with temperature control using the built-in variable temperature module, and samples were equilibrated for at least 5 minutes at specified temperatures prior to the collection of data.

Self-diffusion coefficients for the Li^+ cation and the fluorine-containing anion (STFSI) were obtained using the pulse-gradient stimulated echo (PGSTE) experiment on ^{7}Li and ^{19}F nuclei. The Stejskal–Tanner equation (eqn (1)) was used to fit the integrated peak area as a function of the gradient strength (g).

$$A(g) = A_0 \exp\left(-D\gamma^2 g^2 \delta^2 \left(\Delta - \frac{\delta}{3}\right)\right) \tag{1}$$

In eqn (1), A_0 is the peak area at zero gradient ($g = 0$), $A(g)$ is the peak area at gradient g, γ is the gyromagnetic ratio of the nucleus, δ is the gradient pulse duration, Δ is the diffusion time between gradient pulses, and D is the self-diffusion coefficient. The values of the adjustable parameters (g, δ, and Δ) were selected to achieve ≥85% signal attenuation in at least 16 gradient steps. For the samples in this study, δ was in the range of 1–2 ms, Δ was in the range of 7–30 ms, and the max gradient was $1700\ \mathrm{G\ cm^{-1}}$. The fits of the signal data were performed using Bruker's TopSpin, v. 3.6.4 software using the varB function type with one or two components.

4.7 SEM

Coin cells containing the entire cell stack of NMC622|PE|Li were opened in an Ar-filled glovebox after completion of cycling. Li was gently shaved off from the PE using a razor blade. The NMC622|PE bilayer stack was transferred into a sealed vial and loaded quickly into a Leica EM FC7 cryomicrotome cooled to −80 °C. The cooling chamber of the cryomicrotome was filled with N_2. A flat cross-section was created by microtoming the bilayer stack at −80 °C, with a sectioning thickness of 100 nm at $0.6\ \mathrm{mm\ s^{-1}}$ speed. The flattened cross-section was examined with a Zeiss Merlin SEM, using an acceleration voltage of 10 kV.

4.8 Cryo-STEM and EELS

Similar to SEM sample preparation, the NMC622|PE bilayer stack was transferred into a sealed vial and loaded quickly into a Leica EM FC7 cryomicrotome cooled to −80 °C. Thin sections with a thickness of approximately 100 nm were collected on a lacy carbon coated copper grid. The sectioning speed was $0.2\ \mathrm{mm\ s^{-1}}$. The thin sections were allowed to warm up to room temperature in a N_2 filled chamber, quickly transferred to an Ar-filled glovebox, and stored in the glovebox prior to TEM imaging. The TEM samples were quickly transferred into the TEM sample holder in air and allowed to cool down to near liquid N_2 temperature inside the microscope.

Low-dose, high-resolution electron energy-loss spectroscopy (EELS) was performed on a Thermo Fisher Scientific Titan Krios G4 operated at 300 kV in STEM mode. Spectrum images (SIs) we acquired with electron doses between $5\ e^-\ \text{Å}^{-2}$ and $2 \times 10^2\ e^-\ \text{Å}^{-2}$. To analyze the SIs, custom Python codes were written that utilize common packages such as NumPy, SciPy, *etc.* Standard power-law background subtraction was performed at each probe position, and simultaneous dark-field images were used to generate a binary mask on the NMC particles to establish the location of their surfaces. These binary masks were then dilated and eroded, and differences between the resulting masks were taken to generate new masks that followed the contour of the NMC particle surfaces but that were located within the particles and the surrounding polymer. The average EELS spectrum from each of these areas was then taken to generate a "line profile" of average spectra as a function of distance from the particle surfaces. Further analysis of these line profiles to establish regions with unique spectra was performed by multivariate curve resolution (MCR), which decomposes the data set into spatial and spectral components that can reconstruct the original data at each probe position through a linear combination of the resulting components. The results of this process on the EELS line profiles were then displayed as the spectral components and two-dimensional spatial component maps by appropriately coloring the spectral components and the corresponding surface profiles generated by the binary mask processes.

4.9 Simulations

The microstructure of the cathode was approximated in the following way. The NMC622 single crystal particles were approximated in 2D as rectangles. The values of the long side, a, and the short side, b, of the rectangles were collected from the cross-sectional SEM of the cathode using ImageJ software. The binned histograms together with the Gaussian fits of the long side and the ratio of the sides are shown in Fig. S10a and b. Measuring the two sides as opposed to measuring the diagonal of the particle seems more appropriate since the corners of the particles appear rounded.

The electrode area of 20 × 32 μm was seeded with the particles using the normal probability distribution,

$$p(x) = \frac{1}{\sqrt{2\pi\sigma}} e^{-\frac{(x-\mu)^2}{2\sigma^2}}$$

with the variance, σ^2, and mean, μ, obtained from the measured distributions (Fig. S10a and b). The Box–Muller method was used for normal (Gaussian) distributions symmetric around zero, which were then transposed into the measured mean and variance. The particles were randomly placed in the domain with randomly assigned coordinates of the bottom left corner and rotation of the rectangles. Overlapping particles were merged to form larger agglomerates.

The geometry represented the arrangement in the experiments in 2D. The NMC electrodes were 50 μm thick. The NMC particles were surrounded by a porous binder/carbon black foam filled with the polymer electrolyte and thus capable of conducting both electrons and ions. The rest of the geometry was represented by an 80 μm thick layer of PE, and the counter electrode was modeled as a Li electrode surface. The resulting geometry was meshed with tetrahedral elements (Fig. S10c). The NMC, binder-electrolyte, and electrolyte domains were explicitly resolved with the charge transfer at the NMC particle/binder–electrolyte interface following Butler–Volmer kinetics. This way, the diffusion in the NMC particles as well as diffusion and migration in the electrolyte can be explicitly visualized. In both cases, the diffusion was simplified as isotropic. The experimentally measured diffusivity values in various PEs were utilized (Table S1). Lithium diffusivity in NMC622 was assumed isotropic, constant, and equal to 4×10^{-11} cm^2 s^{-1}.[42] An equivalent of the current density used in the experiments, 32 μA cm^{-2}, was applied to the current collector surface, and the cell charge was simulated until 4.3 V as a stop condition.

Conflicts of interest

There are no conflicts to declare.

Data availability

All data supporting the findings of this study are either included in the article and supporting information (SI) or are available from the corresponding author(s) upon reasonable request. Supplementary information is available. See DOI: https://doi.org/10.1039/d5ta07799k.

Acknowledgements

This research at Oak Ridge National Laboratory, managed by UT-Battelle, LLC, for the U.S. Department of Energy under contract DE-AC05-00OR22725, was primarily sponsored by the U.S. Department of Energy (DOE), Office of Energy Efficiency and Renewable Energy for the Vehicle Technologies Office's Advanced Battery Materials Research Program (Tien Duong and Simon Thompson, Program Managers). The SEM and cryo-STEM/EELS portion of this research was supported by the Center for Nanophase Materials Sciences (CNMS), which is a US Department of Energy, Office of Science User Facility at Oak Ridge National Laboratory, as well as by the Laboratory Directed Research and Development Program of Oak Ridge National Laboratory (ORNL, managed by UT-Battelle, LLC, for the U.S. Department of Energy) under Contract no. DEAC05-00OR22725. Cryo-STEM EELS additionally performed using instrumentation within ORNL's Materials Characterization Core provided by UT-Battelle, LLC, under Contract No. DE-AC05-00OR22725 with the DOE and sponsored by the Laboratory Directed Research and Development Program of Oak Ridge National Laboratory, managed by UT-Battelle, LLC, for the U.S. Department of Energy.

References

1 Y.-S. Hu, Batteries: getting solid, *Nat. Energy*, 2016, **1**(4), 1–2.
2 T. Placke, R. Kloepsch, S. Dühnen and M. Winter, Lithium ion, lithium metal, and alternative rechargeable battery technologies: the odyssey for high energy density, *J. Solid State Electrochem.*, 2017, **21**, 1939–1964.
3 Y. Bae Song, H. Kwak, W. Cho, K. S. Kim, Y. Seok Jung and K.-H. Park, Electrochemo-mechanical effects as a critical design factor for all-solid-state batteries, *Curr. Opin. Solid State Mater. Sci.*, 2022, **26**(1), 100977.
4 S. Kalnaus, N. J. Dudney, A. S. Westover, E. Herbert and S. Hackney, Solid-state batteries: The critical role of mechanics, *Science*, 2023, **381**(6664), eabg5998.
5 M. J. Wang, E. Kazyak, N. P. Dasgupta and J. Sakamoto, Transitioning solid-state batteries from lab to market: Linking electro-chemo-mechanics with practical considerations, *Joule*, 2021, **5**(6), 1371–1390.
6 P. Hovington, M. Lagacé, A. Guerfi, P. Bouchard, A. Mauger, C. M. Julien, M. Armand and K. Zaghib, New Lithium Metal Polymer Solid State Battery for an Ultrahigh Energy: Nano C-LiFePO4 versus Nano Li1.2V3O8, *Nano Lett.*, 2015, **15**(4), 2671–2678.
7 S. Kaboli, H. Demers, A. Paolella, A. Darwiche, M. Dontigny, D. Clément, A. Guerfi, M. L. Trudeau, J. B. Goodenough and K. Zaghib, Behavior of Solid Electrolyte in Li-Polymer Battery with NMC Cathode via in-Situ Scanning Electron Microscopy, *Nano Lett.*, 2020, **20**(3), 1607–1613.
8 K. D. Owensby, R. Sahore, W.-Y. Tsai and X. C. Chen, Understanding and controlling lithium morphology in solid polymer and gel polymer systems: mechanisms, strategies, and gaps, *Mater. Adv.*, 2023, **7**(22), 10271–10280.
9 Y. An, X. Han, Y. Liu, A. Azhar, J. Na, A. K. Nanjundan, S. Wang, J. Yu and Y. Yamauchi, Progress in Solid Polymer Electrolytes for Lithium-Ion Batteries and Beyond, *Small*, 2022, **18**(3), 2103617.
10 D. T. Hallinan and N. P. Balsara, Polymer Electrolytes, *Annu. Rev. Mater. Res.*, 2013, **43**(43), 503–525.
11 M. A. Cabañero Martínez, N. Boaretto, A. J. Naylor, F. Alcaide, G. D. Salian, F. Palombarini, E. Ayerbe, M. Borras and M. Casas-Cabanas, Are polymer-based electrolytes ready for high-voltage lithium battery

applications? An overview of degradation mechanisms and battery performance, *Adv. Energy Mater.*, 2022, **12**(32), 2201264.

12 L. Seidl, R. Grissa, L. Zhang, S. Trabesinger and C. Battaglia, Unraveling the voltage-dependent oxidation mechanisms of poly (ethylene oxide)-based solid electrolytes for solid-state batteries, *Adv. Mater. Interfaces*, 2022, **9**(8), 2100704.

13 Y. Yusim, D. F. Hunstock, A. Mayer, D. Bresser, S. Passerini, J. Janek and A. Henss, Investigation of the Stability of the Poly (ethylene oxide)| LiNi1-x-y CoxMnyO2 Interface in Solid-State Batteries, *Adv. Mater. Interfaces*, 2024, **11**(3), 2300532.

14 H. Zheng, J. Li, X. Song, G. Liu and V. S. Battaglia, A comprehensive understanding of electrode thickness effects on the electrochemical performances of Li-ion battery cathodes, *Electrochim. Acta*, 2012, **71**, 258–265.

15 H. Kim, S. K. Oh, J. Lee, S. W. Doo, Y. Kim and K. T. Lee, Failure mode of thick cathodes for Li-ion batteries: Variation of state-of-charge along the electrode thickness direction, *Electrochim. Acta*, 2021, **370**, 137743.

16 K.-Y. Park, J.-W. Park, W. M. Seong, K. Yoon, T.-H. Hwang, K.-H. Ko, J.-H. Han, Y. Jaedong and K. Kang, Understanding capacity fading mechanism of thick electrodes for lithium-ion rechargeable batteries, *J. Power Sources*, 2020, **468**, 228369.

17 Z. An, T. Shi, Y. Zhao, Q. Gong, D. Zhang, J. Bai and X. Du, Study on aging and external short circuit mechanisms of Li-ion cells with different electrode thicknesses, *Appl. Energy*, 2023, **350**, 121796.

18 J. Ma, Z. Liu, B. Chen, L. Wang, L. Yue, H. Liu, J. Zhang, Z. Liu and G. Cui, A strategy to make high voltage LiCoO2 compatible with polyethylene oxide electrolyte in all-solid-state lithium ion batteries, *J. Electrochem. Soc.*, 2017, **164**(14), A3454.

19 K. Nie, X. Wang, J. Qiu, Y. Wang, Q. Yang, J. Xu, X. Yu, H. Li, X. Huang and L. Chen, Increasing Poly (ethylene oxide) Stability to 4.5 V by Surface Coating of the Cathode, *ACS Energy Lett.*, 2020, **5**(3), 826–832.

20 J. Liang, S. Hwang, S. Li, J. Luo, Y. Sun, Y. Zhao, Q. Sun, W. Li, M. Li and M. N. Banis, Stabilizing and understanding the interface between nickel-rich cathode and PEO-based electrolyte by lithium niobium oxide coating for high-performance all-solid-state batteries, *Nano Energy*, 2020, **78**, 105107.

21 R. Sahore, B. L. Armstrong, X. Tang, C. Liu, K. Owensby, S. Kalnaus and X. C. Chen, Role of Scaffold Architecture and Excess Surface Polymer Layers in a 3D-Interconnected Ceramic/Polymer Composite Electrolyte, *Adv. Energy Mater.*, 2023, **13**(19), 2203663.

22 R. Sahore, K. D. Owensby, B. L. Armstrong, J. Ock, M. L. Lehmann, A. M. Ullman, S. Kalnaus and X. C. Chen, Pathway to High Rate Capability in Interconnected Composite Electrolytes: A Case Study with a Single-Ion-Conducting Polymer, *ACS Appl. Energy Mater.*, 2024, **7**(24), 11714–11723.

23 Z. Du, D. L. Wood, C. Daniel, S. Kalnaus and J. Li, Understanding limiting factors in thick electrode performance as applied to high energy density Li-ion batteries, *J. Appl. Electrochem.*, 2017, **47**, 405–415.

24 R. Sahore, G. Yang, X. C. Chen, W.-Y. Tsai, J. Li, N. J. Dudney and A. Westover, A Bilayer Electrolyte Design to Enable High-Areal-Capacity Composite Cathodes in Polymer Electrolytes Based Solid-State Lithium Metal Batteries, *ACS Appl. Energy Mater.*, 2022, **5**(2), 1409–1413.

25 A. Tornheim, S. Sharifi-Asl, J. C. Garcia, J. Bareño, H. Iddir, R. Shahbazian-Yassar and Z. Zhang, Effect of electrolyte composition on rock salt surface degradation in NMC cathodes during high-voltage potentiostatic holds, *Nano Energy*, 2019, **55**, 216–225.

26 Y. Zhang, Q. Wang, B. Liaw, S. C. Nagpure, E. J. Dufek and C. C. Dickerson, A quantitative failure analysis on capacity fade in rechargeable lithium metal cells, *J. Electrochem. Soc.*, 2020, **167**(9), 090502.

27 L. Stolz, G. Homann, M. Winter and J. Kasnatscheew, The Sand equation and its enormous practical relevance for solid-state lithium metal batteries, *Mater. Today*, 2021, **44**, 9–14.

28 Z. J. Hoffman, A. Mistry, V. Srinivasan and N. P. Balsara, Comparing experimentally-measured sand's times with concentrated solution theory predictions in a polymer electrolyte, *J. Electrochem. Soc.*, 2023, **170**(12), 120524.

29 I. Bloom, S. A. Jones, V. S. Battaglia, G. L. Henriksen, J. P. Christophersen, R. B. Wright, C. D. Ho, J. R. Belt and C. G. Motloch, Effect of cathode composition on capacity fade, impedance rise and power fade in high-power, lithium-ion cells, *J. Power Sources*, 2003, **124**(2), 538–550.

30 H. Zhou, F. Xin, B. Pei and S. Whittingham, What Limits the Capacity of Layered Oxide Cathodes in Lithium Batteries?, *ACS Energy Lett.*, 2019, **4**(8), 1902–1906.

31 K. M. Diederichsen, E. J. McShane and B. D. McCloskey, Promising Routes to a High Li+ Transference Number Electrolyte for Lithium Ion Batteries, *ACS Energy Lett.*, 2017, **2**(11), 2563–2575.

32 M. Doyle, T. F. Fuller and J. Newman, The importance of the lithium ion transference number in lithium/polymer cells, *Electrochim. Acta*, 1994, **39**(13), 2073–2081.

33 K. D. Owensby, J. Ock, R. Sahore, H. M. Meyer III, E. C. Self, Y.-R. Lin, W.-Y. Tsai and X. C. Chen, The Impact of Lithium Anode Interface on Capacity Fade in Polymer Electrolyte-Based Solid-State Batteries, *ACS Appl. Energy Mater.*, 2024, **7**(22), 10271–10280.

34 Z. Qin, T. Zhang, X. Gao, W. Luo, J. Han, B. Lu, J. Zhou and G. Chen, Self-Reconstruction of Highly Degraded LiNi0. 8Co0. 1Mn0. 1O2 toward Stable Single-Crystalline Cathode, *Adv. Mater.*, 2024, **36**(5), 2307091.

35 F. Lin, I. M. Markus, M. M. Doeff and H. L. Xin, Chemical and Structural Stability of Lithium-Ion Battery Electrode Materials under Electron Beam, *Sci. Rep.*, 2014, **4**(1), 5694.

36 F. Lin, I. M. Markus, D. Nordlund, T.-C. Weng, M. D. Asta, H. L. Xin and M. M. Doeff, Surface reconstruction and chemical evolution of stoichiometric layered cathode materials for lithium-ion batteries, *Nat. Commun.*, 2014, **5**(1), 3529.

37 N. Zhang, S. Yu, I. Hamam, B. Tang, M. Johnson and J. Dahn, Long-term cycling and mechanisms of cell degradation of single crystal LiNi0. 95Mn0. 04Co0. 01O2/graphite cells, *J. Electrochem. Soc.*, 2024, **171**(1), 010520.

38 M. n. M. Besli, S. Xia, S. Kuppan, Y. Huang, M. Metzger, A. K. Shukla, G. Schneider, S. Hellstrom, J. Christensen and M. M. Doeff, Mesoscale chemomechanical interplay of the LiNi0. 8Co0. 15Al0. 05O2 cathode in solid-state polymer batteries, *Chem. Mater.*, 2018, **31**(2), 491–501.

39 H.-H. Ryu, B. Namkoong, J.-H. Kim, I. Belharouak, C. S. Yoon and Y.-K. Sun, Capacity Fading Mechanisms in Ni-Rich Single-Crystal NCM Cathodes, *ACS Energy Lett.*, 2021, **6**(8), 2726–2734.

40 M. D. Galluzzo, J. A. Maslyn, D. B. Shah and N. P. Balsara, Ohm's law for ion conduction in lithium and beyond-lithium battery electrolytes, *J. Chem. Phys.*, 2019, **151**(2), 020901.

41 J. Evans, C. A. Vincent and P. G. Bruce, Electrochemical measurement of transference numbers in polymer electrolytes, *Polymer*, 1987, **28**(13), 2324–2328.

42 T. E. Ashton, P. J. Baker, C. Sotelo-Vazquez, C. J. Footer, K. M. Kojima, T. Matsukawa, T. Kamiyama and J. A. Darr, Stoichiometrically driven disorder and local diffusion in NMC cathodes, *J. Mater. Chem. A*, 2021, **9**(16), 10477–10486.